6

Innovative Concepts in Wind-Power Generation: The VGOT Darrieus

Fernando Ponta, Alejandro Otero*, and Lucas Lago
Michigan Technological University
USA

1. Introduction

Considerable progress in wind-power technology during the last decades has made it an important supplier of grid-connected electricity in the world energy picture. Nowadays, wind power is the most rapidly growing and most widely utilized renewable energy technology, with a total of 159.2 GW installed worldwide at the end of 2009 producing 340 TWh per year, which is about 2% of worldwide electricity usage (WWEA, 2010).

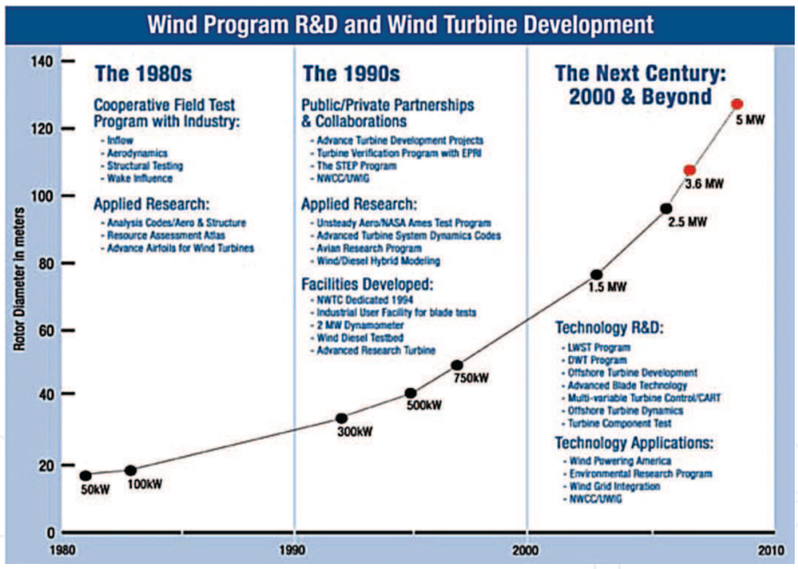

Fig. 1. The wind-turbine upscaling phenomenon (from NREL, 2005).

Over the last 30 years, there has been a spontaneous tendency in the wind-turbine industry to increase the size of the state-of-the-art machine. Figure 1 shows a chart published by NREL-DOE where this upscaling phenomenon is clearly depicted (NREL, 2005). This tendency is driven by economies-of-scale factors that substantially reduce the cost of wind energy. Starting from the typical 50 kW machine of the early 1980s, output power of the state-of-the-art wind turbines is now in the range of 3.6 to 6 MW, with rotor diameters up to

*Also at: FIUBA/CONICET, Buenos Aires, Argentina

127 meters. Commercial models within this range are available from several manufacturers like GE, RE-Power, Enercon, Vestas, and Siemens. In recent years industry insiders have been talking about a next-generation of giant offshore turbines of 7.5 to 12 MW with rotor diameters up to 200 meters (de Vries, 2005). If this generation of superturbines is successfully developed, wind-energy costs would be reduced substantially.

There is still a wide margin for improvement within the current horizontal-axis wind-turbine technology (HAWT), which looks as the most effective way to go in the short- to medium-term future. The development of adaptive-blades with aeroelastic tailoring the flexo-torsional modes of the blade structure to reduce aerodynamic loads, the introduction of a modular-concept blade that could be split into easy-to-handle segments, and the use of advanced materials and manufacturing techniques in blades and other components are only some examples of how to improve the economics of design, manufacturing, transport-logistics, and operation of HAWTs (NREL, 2008). But the HAWT technology would ultimately reach its limits in the long-term future. As sizes increase, a number of related problems would appear in rotor design, transport and assembly. Ultimately, the low rotational speed associated with huge radii would complicate the coupling with the electrical generator to the point that the size and weight of the drive train required would become impractical.

On the other hand, there are geographical regions around the world (e.g. Alaska, British Columbia, Labrador, Patagonia) characterized by vast wind resources. Mean speeds in some areas almost double those recorded at the typical locations for which commercially-available wind turbines were designed. Those regions, classified as outstanding and superb, offer an enormous potential in terms of energy resource where, in the future, it might even be possible to produce hydrogen as a substitute fuel in competitive terms, helping to close the gap between global fuel needs and the maximum amount of biofuel that may be produced sustainably. Hence, it is worthwhile to explore innovative concepts in extra-large wind-power plants to be able to exploit the renewable energetic potential that those regions offer.

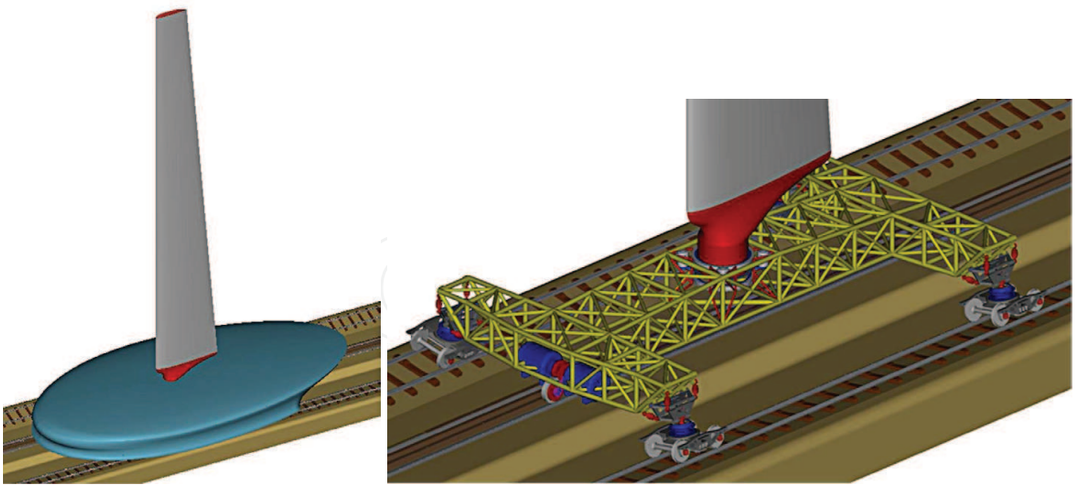

(a) (b)

Fig. 2. Perspective view of a blade-wagon (a). Structural configuration of a blade-wagon showing bogies, suspension system, and the electrical generators coupled to their driving wheels. (b).

In this chapter we are going to explore an innovative concept that, by going beyond the classical evolutive-design process based on the HAWT concept, may help address those challenges in the long-term future of wind-turbine technology. The Variable-Geometry Oval-Trajectory (VGOT) is an innovative type of wind turbine based on the Darrieus-type rotor which has been introduced by Ponta & Luna Pont (1998). In a traditional Darrieus, the blades rotate around a central vertical axis. In the VGOT, instead, each blade slides over rails mounted on a wagon formed by a reticulated structure supported by standard train bogies (see Figure 2). Each wagon contains its own electrical generation system coupled to the power-wheels and the electricity is collected by a classical third rail system (Ponta et al., 2004; 2001; 2002). With the VGOT design, if we keep constant the velocity of the wagons (i.e. the tangential speed of the blades), we can increase the area swept by the blades (and hence the rated power of the plant) without the low-rotational-speed problems associated with a classical Darrieus rotor of large diameter.

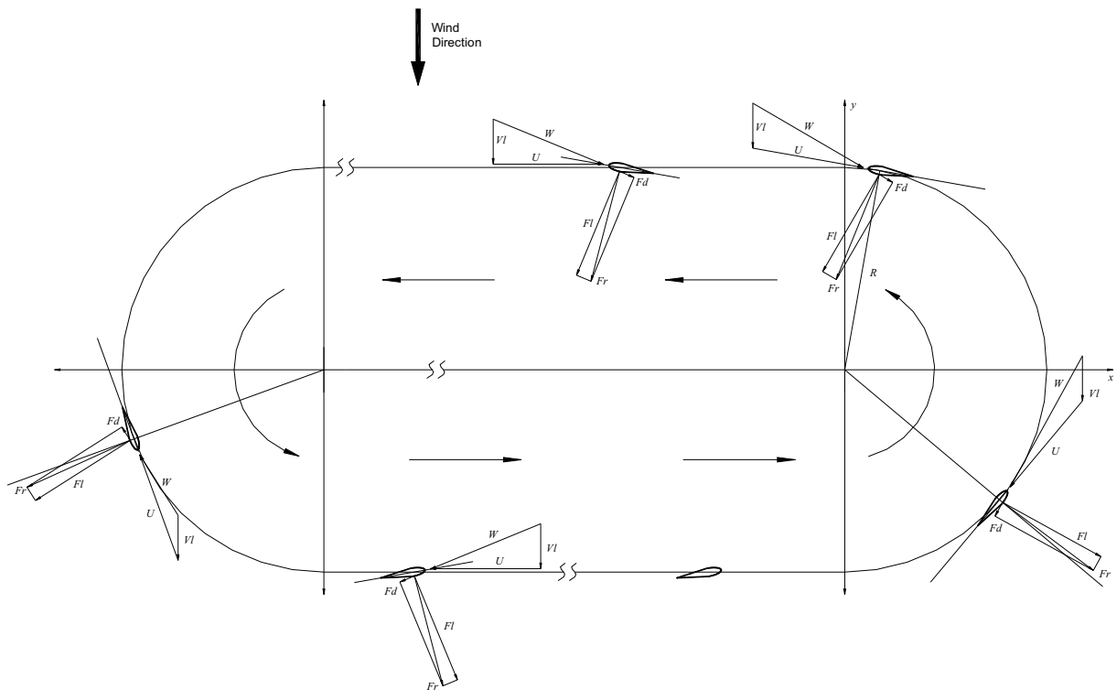

Fig. 3. Schematic view of the path followed by the blade-wagons of the VGOT Darrieus showing the velocity composition of the incoming flow and the aerodynamic forces acting on the blades.

The blade-wagon elements of a VGOT Darrieus, not being solidly affixed to a central axis, could move following a non-circular trajectory (see Figure 3). For certain locations where the compass rose shows a preferential bearing it is possible to optimize the energy-conversion efficiency of the entire plant by increasing the portion of transit perpendicular to the bearing of the incoming wind. Along the perpendicular tracks, the blade generates the higher output-power, while along the portions where the trajectory is in-line with the incoming wind the blade-wagon not only does not produce energy but actually consumes it, taking power from the rest of the plant to keep moving. Thus, extending those portions of the path

perpendicular to the wind by the addition of straight tracks the overall energy-conversion efficiency of the plant increases (Ponta et al., 2007). This configuration also allows for increasing the area swept by the blades (which depends on the blade height and the trajectory width across the direction of the incoming wind), with a smaller increment in the path length compared to a circular trajectory. It reduces investment in rails and blades to get the same output-power. On the other hand, along these straight tracks the direction of inflow on the blades would remain practically constant, contributing to aerodynamic and structural stability of the system. This situation is different from a traditional Darrieus where the blades are subjected to an inflow variable in both magnitude and angle of incidence all along the path.

1.1 Technical features of the VGOT Darrieus

In our design, we looked for the use of normal railway material as much as possible. Rails, sleepers, supporting wheels, and other mechanical devices are intended to be chosen among the standards. As well as electrical generators, third-rail electricity-collecting lines, and other electrical devices are intended to be standard too. Besides, other stock pieces of equipment could be adapted to our purposes and some other devices should be designed specially.

When confronting the study of the structural behaviour of the VGOT Darrieus we found several particularities that distinguish it from other three-dimensional reticulated structures. As mentioned above, each blade is mounted on a chassis supported by standard train bogies and covered by a streamlined case designed to decrease aerodynamic drag (see Figure 2(a)). The chassis is formed by a tubular reticulated structure that should be designed to absorb the efforts in the vertical and traverse directions of the railroad due to the aerodynamic loads, the weight of the components and the centrifugal acceleration along the curved tracks. The effects of the link between the blade and the suspension should be considered, together with the added mass effects of the components and the ballast placed to improve the stability of the wagon. To this end, we developed a computer model to simulate the integral behaviour of the reticulated structure, the suspension, and the blade itself. It involves several subroutines including a finite element code to solve the three-dimensional beam reticulated assemble. Due to its complexity, this code is treated comprehensively in a separate paper, Otero & Ponta (2004).

Each blade-wagon contains its own electrical generation system. The generators are connected to the power wheels by a gear transmission. The wheels are placed at the center of the front part of the chassis (see Figure 2(b)) and draw the power by the friction of the wheels on a ground rail. For this device we propose a twin design based upon a pair of oscillating-lever gearboxes coaxial with the electrical generators. This layout not only drives the torque from the wheels to the electrical machines, but also adjusts the rotational speed to perform a suitable mechanical coupling and keeps a uniform distribution of the weight. The electricity generated is collected by a classical third rail system.

Another interesting feature of the VGOT concept is its relatively long cycle time. It allows the use of a blade-positioning control system that operates continuously during the cycle without the fatigue and mechanical-inertia problems associated with variable-geometry attempts in classical Darrieus rotors. With the addition of an orienting device, the blades could set themselves at an optimal angle with a further increment in the energy-conversion efficiency. Several components of this control system could be taken directly from the standard technology used for nacelle-orientation in classical horizontal-axis wind-turbines. The possibility of a blade-positioning control could help remarkably with the issue of

controlling the speed of the wagons and the distance between them, as well as acting as an effective emergency-halt system.

There are three alternative strategies for the combined generation and blade-positioning system. First is to use *asynchronous generators linking the blade-wagons electrically*. Here, the speed of each generator is fixed by the frequency of the electric line, and due to the steep torque/rotational-speed characteristic curve of the asynchronous generator, it remains close to the synchronous speed. The control system must keep the distance among the generating elements, and also takes charge of the optimum positioning of the blades to maximize the energy-conversion efficiency. Second is to use *asynchronous generators but linking the blade-wagons mechanically*. In this strategy, the speed of the generator of the whole set of wagons is fixed by the frequency of electric line and it remains close to the synchronous speed. The control system takes charge of only the optimum positioning of the blades to maximize efficiency, working as speed-controller only in case of an emergency. Finally, a third alternative would be to use *synchronous generators*. In this case the speed of the wagons is variable and is adjusted with the position of the blade to optimise the conversion efficiency in each case according to the wind conditions. Here the control system must keep the distance among the blade-wagons. Electricity must be converted to DC before transmission through the common third-rail in order to avoid problems of loss of synchronicity between the individual generators while they are adjusting their respective speeds during normal operation.

The suspension system of the VGOT deserves particular attention. Given the particularities of this application, it was necessary to conceive a non-conventional design. The blade-wagon is subject to fluctuating aerodynamic loads in the direction perpendicular to the rails. This means that the suspension system should absorb not only the vertical oscillating loads due to the weight and the irregularities of the rails, but also the cross-rail oscillations induced by the fluctuating aerodynamics. If these loads were transmitted directly to the bogies and the rails, they would compromise the stability of the blade-wagon. The suspension must also adapt itself to follow the imperfections and misalignments in the rails layout, minimizing their effects on the structure and the components. To this end we propose a design based upon a two-axis deformable parallelogram which actions in the lateral and vertical directions by means of a set of spring/shock-absorber units (see Figure 4). This device is complemented with a special cushioned-pin spherical joint that connects the parallelogram to the bogie. This joint allows limited motion in order to let the bogie adjust itself to the eventual misalignments on the rails while its rubber cushion absorbs the inevitable vibrations produced by the imperfections on the railroad.

The concept of mounting a blade on a wagon with the aim of generating electricity has been proposed before (see for example Fig. 1.6, Sec. 1.1.3 Manwell et al., 2002, among others), but no systematic study of its practical possibilities has ever been attempted. With the VGOT concept, we intend to carry on a systematic study of the actual feasibility of such a design. We can schematize the dynamical response of the whole VGOT Darrieus as a combination of three blocks, each one with its own dynamical transference. Namely: the aerodynamic system, the structural system of the wagon's chassis, and the suspension system. In the following sections we are going to analyze each one of these systems in detail.

2. Aerodynamic study of the VGOT Darrieus

When undertaking the study of the aerodynamic behavior of a VGOT Darrieus, several particularities arise that make it different from other studies in vertical-axis wind-turbine aerodynamics. The aerodynamic loads depend on both the position of the blade-wagon

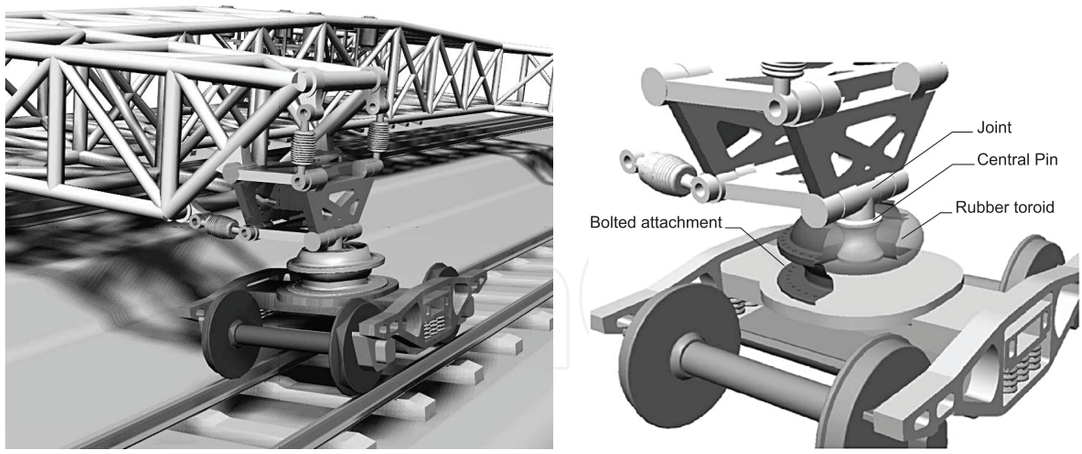

(a) (b)

Fig. 4. Perspective view of the suspension system and cushioned-pin spherical joint that connects the parallelogram to the bogie.(a). Details of the shock absorption mechanism (b).

along the path and the height from the ground. Even though it is composed of a number of individual blades that control their setting angle independently, this plant works as a whole and it is not possible to analyze the aerodynamic behavior of each blade-wagon separately due to the interaction of the adjacent blades. Strictly speaking in terms of its aerodynamics, the VGOT is a vertical-axis multi-blade Darrieus turbine with adaptive setting-angle control.
Since the 1970s several aerodynamic prediction models have been formulated for Darrieus machines. Modelling of these turbines follows two different schools: the streamtube-model approach based upon equating the forces on the rotor blade to the change in streamwise momentum through the rotor, and the vortex-model approach based upon vortex representation of the blades and their wakes. The streamtube approach needs much less computation time but the vortex approach is more accurate. Nevertheless, for a multi-blade machine like the VGOT, the use of a vortex-model approach may become prohibitive in terms of computational cost. The VGOT's number of blades (about a hundred or so), is substantially bigger than the conventional rotors. Representing all those blades and their wakes by a vortex-lattice arrangement would make the computer code extremely slow. On the other hand, the presence of a number of blades uniformly distributed over the cross section of the rotor helps to close the gap between the streamtube model and physical reality. Streamtube models compute the time-average of the forces acting on the blades on the portion of trajectory across the streamtube. This is the equivalent of assuming that there exist an infinite number of blades of infinitesimal chord length in such a way that the product of the number of blades times the chord length (i.e. the solidity) of the real rotor is preserved. In a conventional rotor, the aerodynamic forces are concentrated on the few blades. Conversely, in the multi-blade VGOT they are more uniformly distributed in the many blades along the path, hence the VGOT layout is closer to the ideal assumed by the streamtube-model approach. Another issue to take into account is that the VGOT's big size implies large radii on the curved portions of the trajectory and so low values of the angular speed (ω). That minimizes the so-called curved-flow effect (which depends on ω) which induces error in the streamtube-model calculation of conventional rotors.
Streamtube models have evolved with time and we can distinguish several categories. The first of them is the *single streamtube model* proposed by Templin (1974). It uses a single

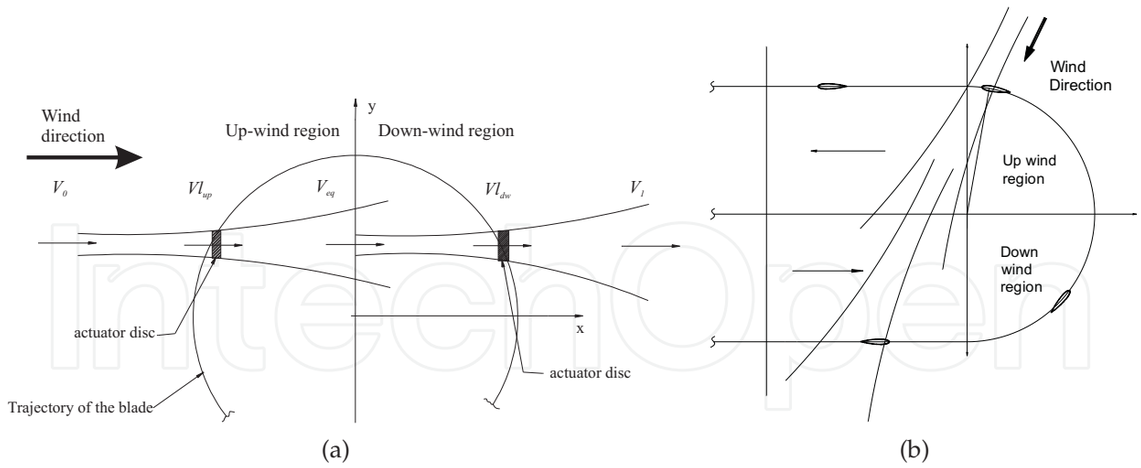

Fig. 5. Double-multiple streamtube model. Schematic view of the tandem arrangement of a double-multiple streamtube (a). Perspective view of the suspension system and cushioned-pin spherical joint that connects the parallelogram to the bogie. Diagram of the dual-scheme streamtube arrangement combining straight and curved tracks. (b).

tube that covers the entire span of the rotor. The rotor's interference is represented by an actuator disk. As the entire rotor is represented by only one tube with one actuator disk, this model predicts a uniform flow for the entire cross section and can not take into account variations of the flow parameters between the upwind and downwind halves of the rotor. To improve the predictive capacities, Strickland (1975) proposed the *multiple streamtube model*, which was also studied by Wilson et al. (1976). It uses an array of adjacent tubes to cover the rotor's span, which takes into account flow variations on the rotor's cross section. A more sophisticated approach called *double-multiple streamtube model* was proposed by Paraschivoiu (1982; 1983a;b). As it uses two actuator disks placed in tandem into each tube of the multiple array (see Figure 5(a)), it can also predict differences between the upwind and downwind halves. Advanced versions of Paraschivoiu's model incorporate dynamic-stall simulation. Streamtube models (specially Paraschivoiu's) can predict effectively the general performance of the rotor (power coefficient vs. tip-speed ratio, power output vs. wind speed, etc.) and their relatively low computational cost makes them a useful practical tool for design. In order to deal with the particular features of the VGOT, we developed a new computational model (see Figure 5(a)) based on the double-multiple streamtube concept that incorporates the capacities of dealing with rotors whose blades follow oval-trajectories at variable setting-angles (Ponta et al., 2007).

As it was mentioned above, the streamtube models are based on the principle of conservation of momentum. The local velocity for each streamtube is computed by equating the average forces on the blades (calculated by the blade element theory using the lift and drag coefficients) to the change in streamwise momentum on the streamtube. From the scheme in Figure 5(a), we have the following relation for the magnitude of the velocity along a double streamtube:

$$V_0 > Vl_{up} > V_{eq} > Vl_{dw} > V_1 \tag{1}$$

where V_0 is the free-stream speed, Vl_{up} and Vl_{dw} the local upstream and downstream velocities, V_{eq} the equilibrium velocity in the coupling of both semitubes, and V_1 is the final velocity in the pseudo-infinite downstream.

The local velocities for each half of the rotor may be written in terms of the velocity at the entrance of each semitube as:

$$Vl_{up} = \xi_{up} V_0, \qquad Vl_{dw} = \xi_{dw} V_{eq} \tag{2}$$

where

$$0 < \xi_{up} < 1, \qquad 0 < \xi_{dw} < 1, \tag{3}$$

are the interference factors for each half of the rotor. From the streamtube theory (see Manwell et al. (2002)), the expression for the local velocity in terms of the inflow and outflow velocities is $Vl = \frac{1}{2}(V_{in} + V_{out})$, then

$$Vl_{up} = \frac{1}{2}\left(V_0 + V_{eq}\right), \tag{4}$$

which gives

$$V_{eq} = \frac{1}{2}\left(2\,\xi_{up} - 1\right) V_0, \tag{5}$$

then

$$\xi_{up} = \frac{Vl_{up}}{V_0}, \qquad \xi_{dw} = \frac{Vl_{dw}}{(2\,\xi_{up} - 1)V_0}. \tag{6}$$

The tip speed ratio is defined as $\lambda_0 = V_p / V_0$, where V_p is the tangential velocity of the moving blade. We may define expressions for the local tip speed ratios:

$$\lambda_{up} = \frac{V_p}{Vl_{up}} = \frac{\lambda_0}{\xi_{up}}, \tag{7}$$

$$\lambda_{dw} = \frac{V_p}{Vl_{dw}} = \frac{\lambda_0}{\xi_{dw}(2\,\xi_{up} - 1)}. \tag{8}$$

From the scheme in Figure 6(a), we have that the inflow velocity on the blades may be expressed as,

$$\left(\frac{W}{Vl}\right)^2 = \left(\frac{Vp}{Vl} + \cos\theta\right)^2 + (\sin\theta)^2 = (\lambda + \cos\theta)^2 + (\sin\theta)^2. \tag{9}$$

We can also obtain the angle of the inflow,

$$\tan\gamma = \frac{\sin\theta}{\frac{Vp}{Vl} + \cos\theta} = \frac{\sin\theta}{\lambda + \cos\theta}, \tag{10}$$

which in terms of the local values gives,

$$\left(\frac{W}{Vl_{up}}\right)^2 = \left(\lambda_{up} + \cos\theta\right)^2 + (\sin\theta)^2, \tag{11}$$

$$\left(\frac{W}{Vl_{dw}}\right)^2 = (\lambda_{dw} + \cos\theta)^2 + (\sin\theta)^2, \tag{12}$$

and

$$\tan\gamma_{up} = \frac{\sin\theta}{\lambda_{up} + \cos\theta}, \qquad \tan\gamma_{dw} = \frac{\sin\theta}{\lambda_{dw} + \cos\theta}. \tag{13}$$

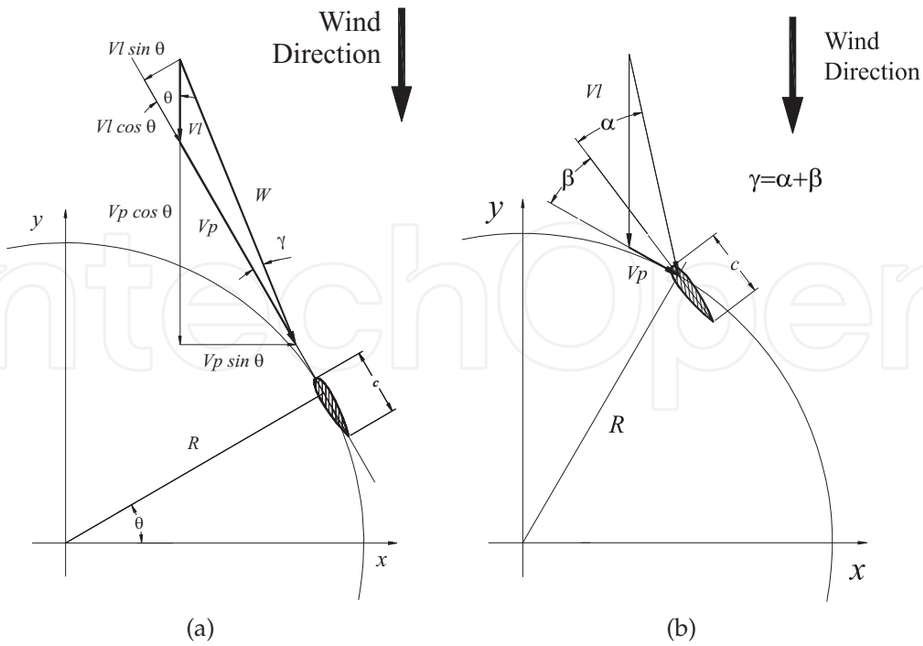

Fig. 6. Comparison of the inflow-velocity diagram for a fixed-geometry Darrieus (a), and a variable-geometry one (b).

For a variable-geometry rotor we have that $\gamma = \alpha + \beta$, where β is the variable setting angle and α is the effective angle of attack on the blade section. Figure 6 illustrates the differences between the velocity diagram for a fixed-geometry Darrieus and a variable-geometry one.
Now, an oval-trajectory Darrieus has two axes of symmetry, thus we have to introduce new concepts which were absent in the standard model for the classical Darrieus rotor. Our model must take into account the angle of the incident wind with respect to the main axis of the oval. We chose to measure the incident-wind angle (φ) from the minor axis of the oval. Earlier versions of our model (Ponta & Seminara, 2000; Seminara & Ponta, 2000) only contemplated four-point compass roses. That is, they just solve the cases where the incidence-wind angle was 0 or 90 degrees (i.e. perpendicular and parallel respectively to the major axis of the oval). It was satisfactory for a first attempt, but it produced too conservative of a prediction of the general performance for winds blowing from a broad range of directions around each side of the mayor axis of the oval. It is of capital importance to determinate the ideal layout of trajectory for a particular compass-rose configuration because the cost-effectiveness of the plant depends on it. Thus, we developed an improved version of the model (Ponta & Seminara, 2001; Seminara & Ponta, 2001) that could deal with those winds blowing from intermediate directions which the previous versions underestimated. To this end, we introduced a dual-scheme streamtube arrangement (see Figure 5(a)) which has the capacity of combining curved and straight tracks for every double-streamtube in order to deal with incident winds blowing from any bearing of the compass.
We also had to introduce a shape coefficient (CF) which defines a proportional relation between the radius of the curved portions of the trajectory and the length of the straight tracks. In this way, we may do changes in the trajectory layout and evaluate the resulting performance under different wind conditions. Another particular aspect that we had to contemplate was the definition of a new system of coordinates to describe the motion of the blades. For an oval

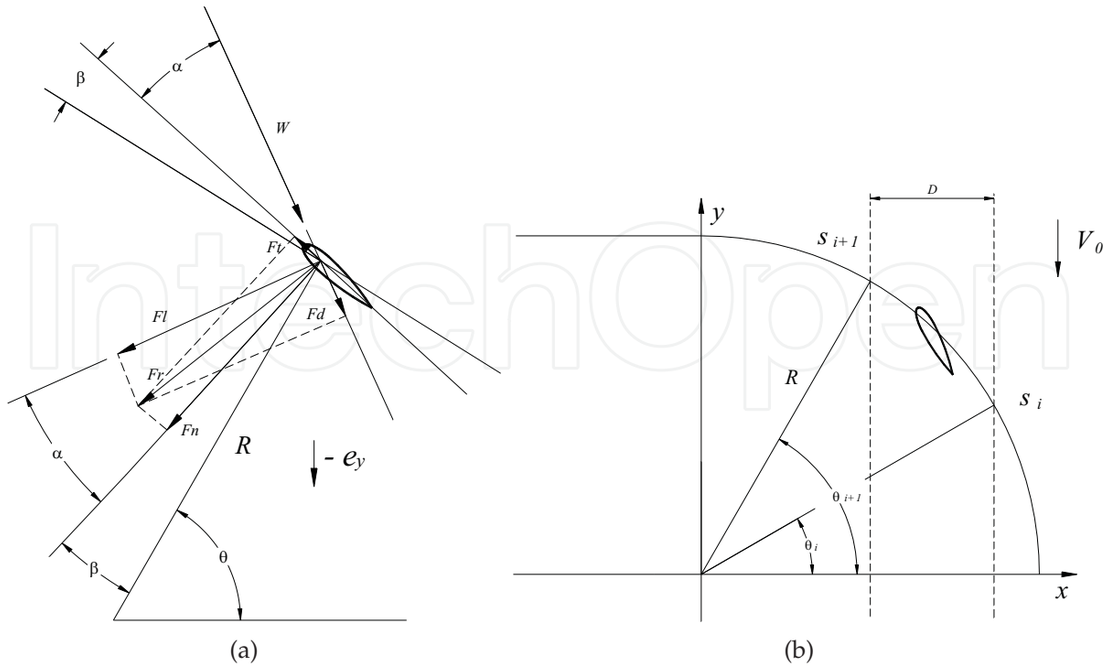

Fig. 7. Diagram of the aerodynamic forces acting on the blades (a). An example of calculation of the width for an upwind tube at $\varphi = 0$ (b).

machine it is no longer possible to simply refer the blade motion to the instant angle along the cycle as in a conventional Darrieus. Hence, we define a new parametric coordinate (s), which describes the motion of the blade and from which its position and the instant angle of its trajectory are computed. Figure 7(b) shows a diagram of the oval trajectory described by the parametric coordinate s.

Figure 7(a) shows a diagram of the aerodynamic forces acting on the blades. From the blade-element theory we calculate that the average value of the aerodynamic force acting on a set of blades passing across a generic streamtube is:

$$F = \frac{N\Delta s}{s_{total}} \frac{1}{\Delta s} \int_{s_i}^{s_{i+1}} \int_{z_j}^{z_{j+1}} \frac{1}{2}\rho W^2 c \left(C_n \sin\left(\theta - \beta + \varphi\right) - \right. \tag{14}$$

$$\left. - C_t \cos\left(\theta - \beta + \varphi\right) + C_{d_o} \cos\left(\theta + \varphi\right)\right) \, dz \, ds \tag{15}$$

where N is the total number of blades, $s_{total} = 2(\pi + CF)R$ is the total length of the trajectory, $\Delta s = s_{i+1} - s_i$ is the length of the portion of trajectory across each tube, z_{j+1} and z_j are the lower and upper heights of the streamtube, C_t and C_n are the Lilenthal's coefficients, and C_{d_o} is the drag coefficient of the wagon (i.e. the aerodynamic drag exerted on the wagon's chassis itself).

On the other hand, from the classical theory of fluid mechanics we have that the axial force acting on a generic streamtube due to the change of momentum is:

$$F = \rho \, A \, Vl \left(V_{in} - V_{out}\right) = 2\rho \, D \, b \, Vl^2 \, \frac{(1 - \xi)}{\xi} \tag{16}$$

where A is the area of the actuator disc placed in the middle of the streamtube, which can be written in terms of its height $b = z_{j+1} - z_j$ and its width D (see an example for an upwind tube at $\varphi = 0$ in Figure 7(b)).
Equating expressions (15) and (16), and after some algebra, we have the general expression of the interference factor for a generic streamtube:

$$\frac{(1-\xi)}{\xi} = \frac{N\,c_m}{8(\pi+CF)\,R\,D} \int_{s_i}^{s_{i+1}} \left(\frac{W}{Vl}\right)^2 (C_n \sin(\theta-\beta+\varphi) - \\ -C_t \cos(\theta-\beta+\varphi) + C_{d_o} \cos(\theta+\varphi))\; ds, \tag{17}$$

where c_m is the average value of the blade-chord length along the height of the streamtube. Combining expressions (8), (11), (12) and (17), we have the following expression for the upstream interference factor:

$$\frac{(1-\xi_{up})}{\xi_{up}} = \frac{N\,c_m}{8(\pi+CF)R\,D} \int_{s_i}^{s_{i+1}} \left(\left(\frac{\lambda_0}{\xi_{up}} + \cos(\theta+\varphi)\right)^2 + (\sin(\theta+\varphi))^2\right) \\ \left(C_n \sin(\theta-\beta+\varphi) - C_t \cos(\theta-\beta+\varphi) + C_{d_o} \cos(\theta+\varphi)\right) ds, \tag{18}$$

and for the downstream one:

$$\frac{(1-\xi_{dw})}{\xi_{dw}} = \frac{N\,c_m}{8(\pi+CF)R\,D} \int_{s_i}^{s_{i+1}} \left(\left(\frac{\lambda_0}{\xi_{dw}(2\xi_{up}-1)} + \cos(\theta+\varphi)\right)^2 + (\sin(\theta+\varphi))^2\right) \\ \left(C_n \sin(\theta-\beta+\varphi) - C_t \cos(\theta-\beta+\varphi) + C_{d_o} \cos(\theta+\varphi)\right) ds, \tag{19}$$

We may compute the local interference factors solving 18 and 19 numerically for each streamtube. We use a combination of subroutines: cubic-spline for interpolation of the aerodynamic coefficients, Newton-Cotes for integration and Newton-Rapson to solve the nonlinear functions. From the interference factors we computed the instantaneous value of the upstream and downstream local velocities. Then, the power coefficient may be calculated as,

$$Cp = \frac{N\,\lambda_0}{2(\pi+CF)(2+CF\cos\varphi)R^2} \sum_{j=1}^{nth} {c_m}^j \sum_{i=1}^{nt} \int_{s_i}^{s_{i+1}} \left(\left(\lambda_0 + {\xi_{up}}^{ij}\cos(\theta+\varphi)\right)^2 + \right. \\ + \left({\xi_{up}}^{ij}\sin(\theta+\varphi)\right)^2 + \left(\lambda_0 + {\xi_{dw}}^{ij}\left(2{\xi_{up}}^{ij}-1\right)\cos(\theta+\varphi)\right)^2 + \\ \left. + \left({\xi_{dw}}^{ij}\left(2{\xi_{up}}^{ij}-1\right)\sin(\theta+\varphi)\right)^2\right) (C_n \sin\beta + C_t\cos\beta - C_{d_o})\, ds, \tag{20}$$

where nth is the total number of streamtubes in height and nt the total number of streamtubes in width.

2.1 Especial parameters

Due to the especial geometric characteristics of the VGOT Darrieus, it was necessary to propose three new non-dimensional parameters to quantify its performance under different wind conditions: the equivalent power coefficient, the equivalent solidity coefficient and the trajectory efficiency. The two former are the corresponding extensions to the VGOT case of the classical solidity and power coefficients of standard turbines. For the equivalent power coefficient we have

$$Cp_{eq} = \sum_{j=1}^{npcr} f_{\%}{}^{j}\, Cp_j, \tag{21}$$

where $f_{\%}{}^{j}$ is the frequency of occurrence of the wind blowing from the j^{th} bearing in the compass rose, Cp_j is the power coefficient for an incident-wind angle corresponding to the j^{th} bearing, and $npcr$ is the total number of bearings in the wind compass rose. For the equivalent solidity coefficient we have

$$\sigma_{eq} = \frac{N\, c_m}{\left(1 + \frac{CF}{\pi}\right) R}. \tag{22}$$

Note that expression (22) converges to its classical counterpart for conventional Darrieus rotors when $CF \to 0$ (i.e. for a circular-trajectory layout).

The third parameter is a completely new conception exclusive for VGOT machines. The trajectory efficiency is an indicator of the economic efficiency of a particular configuration (i.e. a trajectory layout). It relates the total efficiency of energy conversion with the investment on rails and blades. The former is given by the product of the frequency of occurrence of a certain bearing, times the correspondent power coefficient, times the width of the respective swept area, and the latter is proportional to the total length of the path. The expression for the trajectory efficiency is

$$\mathrm{Ef} = \sum_{j=1}^{npcr} \frac{f_{\%}{}^{j}\, Cp_j\, (2 + CF\cos(\varphi_j))}{2(\pi + CF)}. \tag{23}$$

2.2 Numerical Results

In this section we include some numerical results of the application of our model. We first tested different configurations of oval-trajectory rotors with a fixed trajectory layout of $CF = 8$. Figure 8(a) shows the power-coefficient curves at $\varphi = 0$ for different values of equivalent solidity obtained by changing the number of blades.

Next, we tested several rotor configurations changing CF (i.e. the trajectory layout) and the number of blades in such a way of keeping constant the equivalent solidity. Figure 8(b) shows the corresponding power-coefficient curves. We repeated the test for both extreme cases of incident-wind angle $\varphi = 0$ and $\varphi = 90$ (i.e. when the wind blows, perpendicular and parallel to the mayor axis of the oval trajectory).

To study the aptitude of a particular shape under specific wind conditions, we have computed the equivalent power coefficient and the trajectory efficiency for different compass roses. Three artificially-constructed wind conditions that illustrate the extreme cases at which a VGOT Darrieus with its mayor axis oriented in a North-South direction could be subjected. Compass Rose 1 corresponds to winds with a preferential bearing aligned with the minor axis of the oval, Compass Rose 3 to winds with no preferential bearing, and Compass Rose 4 to winds with a preferential bearing aligned with the mayor axis. This series is completed with Compass Rose 2, which corresponds to the real case of the region of Comodoro Rivadavia in Patagonia, which has a strong west-east directionality.

Figures 9(a) and 9(b) show the values of equivalent power coefficient and the trajectory efficiency for a series of VGOT rotors of different shape. All the rotors have a fixed solidity $\sigma_{eq} = 0.6767$ (which is a typical value for this kind of machine), and work at a tip speed ratio $\lambda = 2.2$ which gives the optimum value for that solidity.

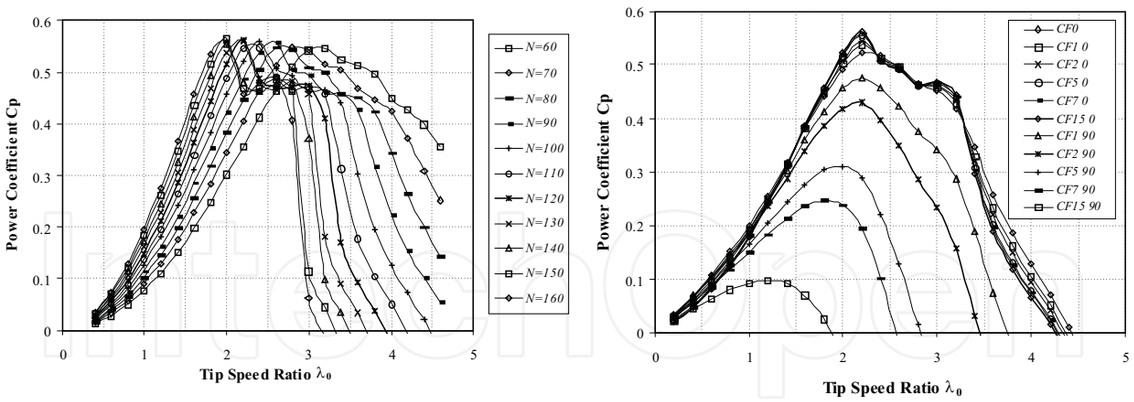

(a) (b)

Fig. 8. Power-coefficient curves at $\varphi = 0$ for VGOT rotors with different number of blades and $CF = 8$ (a). Power-coefficient curves at $\varphi = 0$ and $\varphi = 90$ for VGOT rotors with different trajectory layout but constant solidity (b).

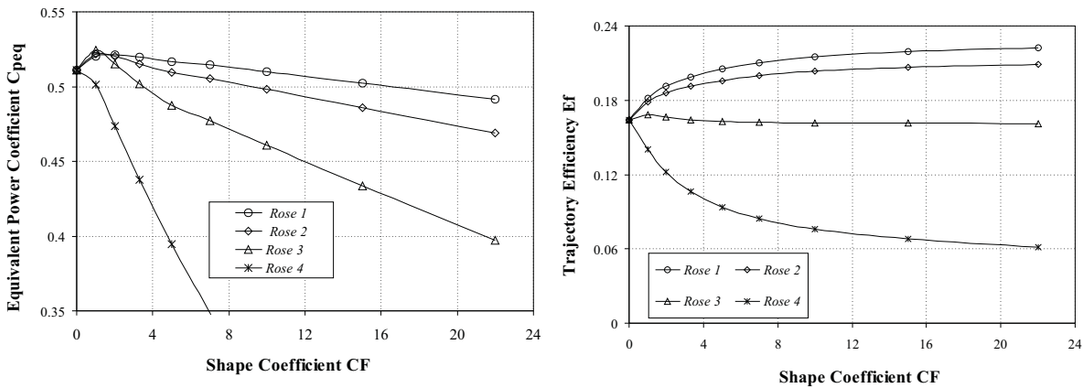

(a) (b)

Fig. 9. Power-coefficient curves for a series of VGOT rotors of different shape under four representative wind conditions (a). Trajectory-efficiency curves for a series of VGOT rotors of different shape under four representative wind conditions (b).

Finally, we computed the aerodynamic loads which were applied to the blade as a distributed load per unit-length. These loads varied in function of both the wagon position along the path and the height from the ground, Figures 10(a) and 10(b) show the aerodynamic load per unit-length in the chord-wise and chord-normal directions (f_{chws}, f_{chnor}) for different heights along the blade in function of the parametric position along the path (i.e. s goes from 0 to 1 to complete the cycle). These data are used as input for a forthcoming study of the structural behavior of the blade-wagon.

3. The structural problem

For the structural study of the blade-wagon, we used a linear analysis approach (i.e. small displacements, small deformations and linear-elastic homogeneous material were assumed). This analysis will be very precise in normal operational conditions at rated power where real

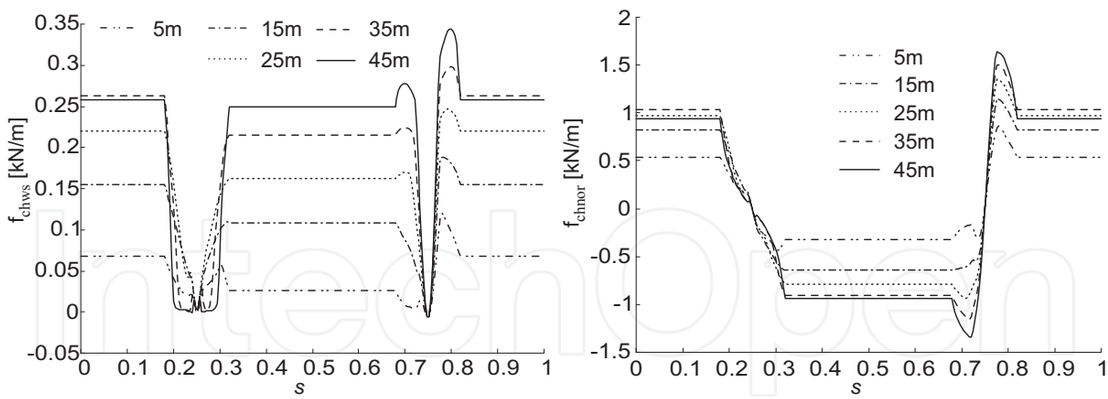

Fig. 10. Aerodynamic load for different heights along the blade span: (a) in the chord-wise direction and (b) in the chord-normal direction.

work conditions fulfil the proposed hypothesis. This linear analysis provides an essential tool for project purposes and serves as the first step for a future study on the non-linear behaviours that are likely to appear when the plant is working at extreme operational conditions.

We used beams and bars to represent the reticulated structure of the wagon, the blade and the suspension. The blade was modelled by 50 variable-section beam elements; the blade-section chord length varies from 8 meters at the bottom to 4 meters at the tip. Each tubular beam of the three-dimensional reticulated structure of the wagon was modelled by one beam element of constant section. Depending on which portion of the structure the beam belonged to, the exterior and interior diameters differ according to design. The details of the suspension system mechanism are going to be studied in the following section. For the purpose the structural study, the behaviour of the suspension system mechanism can be satisfactorily modelled by an assembly of four two-node bar elements. One assembly was located at each one of the four ends of the wagon in place of the actual suspension mechanism. This helps us determine the overall stiffness required from the suspension system in order to keep the stability of the wagon and the aerodynamic configuration. Another mechanism that should be modelled to study the whole structural group of the generating wagon is the blade attachment. This device should link the blade bottom with the reticulated structure and also include the positioning mechanism. It was modelled by beam elements of extremely high stiffness which is quite realistic considering that stiffness is a characteristic inherent to the functionality of this device.

The structure of the VGOT-Darrieus is mainly subject to loads of aerodynamic origin. As mentioned above, aerodynamic loads were calculated by means of a Double-Multiple Streamtube Model and were applied to the blade as a distributed load per unit-length. These loads varied in function of both the wagon position along the path and the height from the ground, figures 10(a) and 10(b) show the aerodynamic load per unit-length in the chord-wise and chord-normal directions (f_{chws}, f_{chnor}) for different heights along the blade in function of the parametric position along the path s. The distributed loads acting on the blade are obtained by projecting f_{chws} and f_{chnor} onto a global system of coordinates aligned with the rails. We also considered loads due to the weight of the chassis, the blade, and the mechanical devices, and also inertial loads due to the centrifugal acceleration. The geometrical boundary conditions apply onto the suspension support points where

displacement is restricted in vertical and transverse directions. Being this i a support bond, bond reactions act only in one sense (i.e. pressing the wheels against the rails) and it was necessary to verify that contact was always preserved. In those cases where this condition was not fulfilled, the ballast was modified to increase the wagon's stability. To take into account the effects of eventual imperfections and misalignment of the rails due to ageing, we introduced randomly-simulated displacements of the points of the structure where the wheels are attached. Displacements in the vertical and transverse directions may be assumed to have a normal statistical distribution with well-known mean and standard deviation. The combination of random displacements that produced the highest stress at each position along the path was selected for evaluation of the effect of rail imperfections.
In order to characterize the structural behaviour of the VGOT Darrieus Rotor, we defined a set of representative parameters: The *Von Misses-yielding stress ratio* ($\sigma_{\mathrm{VM}}/\sigma_{\mathrm{y}}$), which indicates the load state, measured in six witness beams including the beams where the maximum and minimum $\sigma_{\mathrm{VM}}/\sigma_{\mathrm{y}}$ were observed. *Blade-tip transverse displacement* (Δ_{trav}), computed and decomposed in three components: one due to the action of the suspension system, a second due to the deformation of the chassis, and the third due to the lateral bending of the blade. This parameter is useful to ponder the effect of the structure/suspension response on the setting of the blade and check that the aerodynamic configuration is not substantially altered. Finally, the *Blade-tip torsion angle* (ϕ), computed in order to check that the angle of attack of the inflow onto the blade (hence, the aerodynamic load) is not substantially altered.

3.1 Finite element implementation

As mentioned above, we used beams and bars to represent the reticulated structure of wagon chassis, blade, and suspension. We used 3-node isoparametric finite elements with quadratic interpolation assuming Timoshenko beam hypothesis to deal with shear and bending. Torsional and axial effects were included following the classical theory for bars.
The basic expression for the Hellinger-Reissner Functional (see Bathe, 1996, section 4.4.2) leads to a mixed formulation with displacement and strain as independent variables. For the particular case of Timoshenko beams with linear elastic isotropic material, we have the strain tensor $\boldsymbol{\varepsilon} = [\,\varepsilon_{zz}\ \gamma_{zx}^{AS}\ \gamma_{yz}^{AS}\,]^T$, where coordinate z is aligned with the axis of the beam. γ_{yz}^{AS} and γ_{zx}^{AS} represent the distortion due to shear effects in yz and zx planes (the superscript AS denotes that the distortions due to shear will be "assumed" with linear variation along the element length and constant on each cross section). The actual strains given by the strain-displacement relations are $\partial_{\boldsymbol{\varepsilon}}\mathbf{u} = [\,\varepsilon_{zz}\ \gamma_{zx}\ \gamma_{yz}\,]^T$, with $\gamma_{zx} = \frac{du_1}{dz} - \theta_2$ and $\gamma_{yz} = \frac{du_2}{dz} + \theta_1$, where θ_1 and θ_2 are the angles of rotation of the cross section of the beam in the yz and zx planes respectively, and u_1 and u_2 are the displacements in x and y. $\boldsymbol{\theta} = [\,\theta_1\ \theta_2\ \theta_3\,]$ and $\mathbf{u} = [\,u_1\ u_2\ u_3\,]$ together form the so-called *generalized displacements* which are the primitive unknowns to be interpolated quadratically. The stress-strain relations involve the Young and shear moduli of the material, E and G respectively. Then, the expression for the Hellinger-Reissner functional reduces to

$$\Pi^{**} = \int_V \left(\frac{1}{2}\varepsilon_{zz}\, E\, \varepsilon_{zz} - \frac{1}{2}\gamma_{zx}^{AS}\, G\, \gamma_{zx}^{AS} - \frac{1}{2}\gamma_{yz}^{AS}\, G\, \gamma_{yz}^{AS} + \gamma_{zx}^{AS}\, G\, \gamma_{zx} + \gamma_{yz}^{AS}\, G\, \gamma_{yz} \right) \mathrm{d}V - \int_V \left(\mathbf{u}^T \mathbf{f}^B \right)\, \mathrm{d}V\ - \int_{S^f} \left(\mathbf{u}^{S_f} \right)^T \mathbf{f}^{S_f}\, \mathrm{d}S. \tag{24}$$

Under the linear hypothesis we started from, it is possible to add to (24) the contribution of the axial and torsional loads, arriving to the final expression

$$\begin{aligned}\Pi^{**} =& \frac{E}{2}\int_L \Bigg[\underbrace{I_x\left(\frac{d\theta_1}{dz}\right)^2 + I_y\left(\frac{d\theta_2}{dz}\right)^2}_{(i)} + \underbrace{A\left(\frac{du_3}{dz}\right)^2}_{(ii)}\Bigg]\,\mathrm{d}z \\ &+ \frac{G}{2}\int_L \Bigg[\underbrace{-A\left(k_x\left(\gamma_{zx}^{AS}\right)^2 + k_y\left(\gamma_{yz}^{AS}\right)^2\right)}_{(iii)} \\ &\quad + \underbrace{2\,A\left(k_x\,\gamma_{zx}^{AS}\left(\frac{du_1}{dz}-\theta_2\right) + k_y\,\gamma_{yz}^{AS}\left(\frac{du_2}{dz}+\theta_1\right)\right)}_{(iii)} + \underbrace{I_p\left(\frac{d\theta_3}{dz}\right)^2}_{(iv)}\Bigg]\,\mathrm{d}z \\ &\underbrace{- \int_L \mathbf{u}^T\mathbf{p}\,\mathrm{d}z - \int_L \boldsymbol{\theta}^T\mathbf{m}\,\mathrm{d}z - \sum_i \left(\mathbf{u}^i\right)^T\mathbf{F}^i - \sum_j \left(\boldsymbol{\theta}^j\right)^T\mathbf{M}^j}_{(v)}\end{aligned} \tag{25}$$

where I_x, I_y, I_p and A are respectively the inertia and polar moments and the area of the section. k_x and k_y are the shear correction factors (in this case we assumed $k_x = k_y = 1$); $\mathbf{p}$, $\mathbf{m}$, $\mathbf{F^i}$ and $\mathbf{M^j}$ are respectively the distributed and concentrated loads and moments, and L is the length of the beam. Terms in (25) marked as (i) are associated to bending, term (ii) is associated to axial loads, those marked as (iii) are associated to shear, term (iv) is associated to torsion, and the last terms marked as (v) correspond to the external loads and moments.

We discretized the generalized displacements using 1D isoparametric 3-node-element interpolation (see Bathe (1996); Kwon & Bang (1997)). The interpolated displacements and rotations in the j^{th} direction in terms of displacements u_j^i and rotations θ_j^i and the interpolation functions $h_i(r)$ corresponding to node i are $u_j(r) = h_i(r)\ u_j^i$ and $\theta_j(r) = h_i(r)\ \theta_j^i$, where the repeated index indicates summation on the 3 nodes and r is the intrinsic coordinate along the beam element. For the displacement and rotation derivatives with respect to the local coordinate z, we have $\frac{du_j}{dz}(r) = J^{-1}\frac{dh_i}{dr}u_j^i$ and $\frac{d\theta_j}{dz}(r) = J^{-1}\frac{dh_i}{dr}\theta_j^i$.

These magnitudes are then re-written in matrix form as $u_j(r) = \mathbf{H}_{u_j}\ \hat{\mathbf{u}}$, $\frac{du_j}{dz}(r) = \mathbf{B}_{u_j}\ \hat{\mathbf{u}}$, $\theta_j(r) = \mathbf{H}_{\theta_j}\ \hat{\mathbf{u}}$ and $\frac{d\theta_j}{dz}(r) = \mathbf{B}_{\theta_j}\ \hat{\mathbf{u}}$, where $\hat{\mathbf{u}}$ is the array of nodal values of the generalized displacements, and $\mathbf{H}$ and $\mathbf{B}$ are the arrays of interpolation functions and their derivatives in matrix form respectively.

We used 3-point Gaussian integration for the terms interpolated by quadratic functions Bathe (1996); Burden & Faires (1998).

In order to avoid locking problems we used discontinuous linear interpolation for γ_{zx}^{AS} and γ_{yz}^{AS} with 2-point Gaussian integration and condensation at element level. A detailed description of this technique can be found in Bathe (1996). Distortion interpolation can be expressed in matrix form as $\gamma_{zx}^{AS} = \mathbf{H}_{\gamma_{zx}}\boldsymbol{\gamma}^{AS}$ and $\gamma_{yz}^{AS} = \mathbf{H}_{\gamma_{yz}}\boldsymbol{\gamma}^{AS}$, where $\boldsymbol{\gamma}^{AS}$ is the array with the values for the distortion at the integration points while $\mathbf{H}_{\gamma_{zx}}$ and $\mathbf{H}_{\gamma_{yz}}$ are the corresponding arrays of interpolation functions.

Substituting the variables in (25) by their discretized counterparts and invoking the stationarity of the functional, we have

$$\begin{bmatrix} \mathbf{K}_{uu} & \mathbf{K}_{u\gamma} \\ \mathbf{K}_{\gamma u} & \mathbf{K}_{\gamma\gamma} \end{bmatrix} \begin{bmatrix} \hat{\mathbf{u}} \\ \gamma^{AS} \end{bmatrix} = \begin{bmatrix} \mathbf{P} \\ \mathbf{0} \end{bmatrix} \tag{26}$$

where

$$\mathbf{K}_{uu} = E \int_{-1}^{1} \left(I_x \, \mathbf{B}_{\theta_1}^T \, \mathbf{B}_{\theta_1} + I_y \, \mathbf{B}_{\theta_2}^T \, \mathbf{B}_{\theta_2} + A \, \mathbf{B}_{u_3}^T \, \mathbf{B}_{u_3} \right) \, |J| \, \mathrm{d}r + G \int_{-1}^{1} I_p \, \mathbf{B}_{\theta_3}^T \, \mathbf{B}_{\theta_3} \, |J| \, \mathrm{d}r,$$

$$\mathbf{K}_{\gamma u} = \mathbf{K}_{u\gamma}^T = G \int_{-1}^{1} A \, \left[\mathbf{H}_{\gamma_{zx}}^T \, \left(\mathbf{B}_{u_1} - \mathbf{H}_{\theta_2} \right) + \mathbf{H}_{\gamma_{yz}}^T \, \left(\mathbf{B}_{u_2} + \mathbf{H}_{\theta_1} \right) \right] \, |J| \, \mathrm{d}r,$$

$$\mathbf{K}_{\gamma\gamma} = - G \int_{-1}^{1} A \, \left(\mathbf{H}_{\gamma_{zx}}^T \, \mathbf{H}_{\gamma_{zx}} + \mathbf{H}_{\gamma_{yz}}^T \, \mathbf{H}_{\gamma_{yz}} \right) \, |J| \, \mathrm{d}r,$$

$$\mathbf{P} = \int_{-1}^{1} \left[\left(\mathbf{H}_{u_1} + \mathbf{H}_{u_2} + \mathbf{H}_{u_3} \right)^T \widehat{\mathbf{p}} + \left(\mathbf{H}_{\theta_1} + \mathbf{H}_{\theta_2} + \mathbf{H}_{\theta_3} \right)^T \widehat{\mathbf{m}} \right] \, |J| \, \mathrm{d}r + \sum_i \widehat{\mathbf{F}}^i + \sum_j \widehat{\mathbf{M}}^j,$$

$\widehat{\mathbf{p}}$, $\widehat{\mathbf{m}}$, $\widehat{\mathbf{F}}^i$ and $\widehat{\mathbf{M}}^j$ are the corresponding nodal values for the distributed and concentrated loads and moments.

The degrees of freedom associated with γ^{AS} can be condensed at element level. From the second row of (26), we have $\gamma^{AS} = -\mathbf{K}_{\gamma\gamma}^{-1} \, \mathbf{K}_{\gamma u} \, \hat{\mathbf{u}}$, and substituting for γ^{AS} in the first row of (26), it yields

$$\underbrace{\left(\mathbf{K}_{uu} - \mathbf{K}_{u\gamma} \, \mathbf{K}_{\gamma\gamma}^{-1} \, \mathbf{K}_{\gamma u} \right)}_{\mathbf{K}_{el}} \, \hat{\mathbf{u}} = \mathbf{P}. \tag{27}$$

Now, matrix $\mathbf{K}_{el}$ and array $\mathbf{P}$ are transformed from the local coordinates of the beam element to the global coordinates of the structure and assembled into a global matrix $\tilde{\mathbf{K}}$ and load array $\tilde{\mathbf{P}}$ by the standard procedure used in finite-element theory, arriving to the final system

$$\tilde{\mathbf{K}} \, \tilde{\mathbf{U}} = \tilde{\mathbf{P}}, \tag{28}$$

where $\tilde{\mathbf{U}}$ is the global array of nodal values of the generalized displacements. We then follow the classical procedure to impose the geometrical boundary conditions (see Bathe (1996)) and solve the system of equations to obtain the generalized displacements.

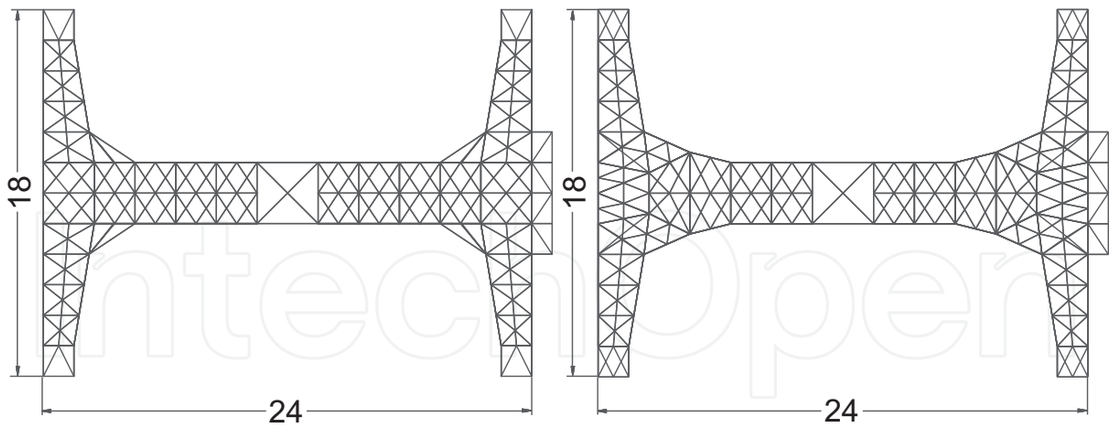

(a) (b)

Fig. 11. Top views of (a) Configuration A and (b) Configuration B. Geometrical coordinates given in meters.

3.2 Numerical Results

After a preliminary study on the basic structural outline (Otero & Ponta, 2002; Ponta & Otero, 2002), we systematically applied our computational code simulating three different configurations for the complete structure of the wagon (chassis, blade and suspension). The combined structural response of each configuration for different positions along the path was analyzed and compared, and the design evolved to improve its performance. We assumed for the three configurations that the curved tracks have a 350-meters radius. We started from Configuration A (see figure 11(a)) deriving the other two in order to improve different aspects of the structural behaviour.

One of the aspects to improve was the stress state of the beams at different zones of the structure. Figure 12(a), shows σ_{VM}/σ_y for 6 witness beams (including the beams which show the maximum and minimum). Maximum σ_{VM}/σ_y was about 60 %, several beams exceed 30 % on some point along the path while there were many that did not even reach 20 % at any point. This dispersion indicates an inadequate distribution of material for the different portions of the chassis and a redesign of the structure was recommendable.

Figure 11(b) shows the modified design of Configuration B. By redesigning the thickness of the beams according to the results obtained for the stress distribution in Configuration A, we achieved a substantial reduction in the maximum stress without increasing the total weight. Figure 12(b) shows a comparison of the maximum stress for the three configurations studied; the reduction in maximum stress between configurations A and B is clearly depicted.

A second aspect to consider during the redesign was the reduction of the transverse displacement shown by the blade tip in Configuration A. We started by analyzing the contribution of each major structural component (the blade, the suspension and the chassis) to the total transverse displacement of the blade tip Δ_{trav}. Figure 13(a) shows the total value of Δ_{trav}, together with the contribution of the three major structural components. We reduced the contribution of the suspension by modifying the stiffness of the springs in the front and back wheels. The deflection of the blade was reduced by redesigning the upper blade structure in order to reduce the top-mass affected by the centrifugal force. To reduce the chassis contribution, we reinforced the zones of the structure where the transverse arms are attached to the longitudinal body of the chassis, which could be noticed by comparing figures 11(a)

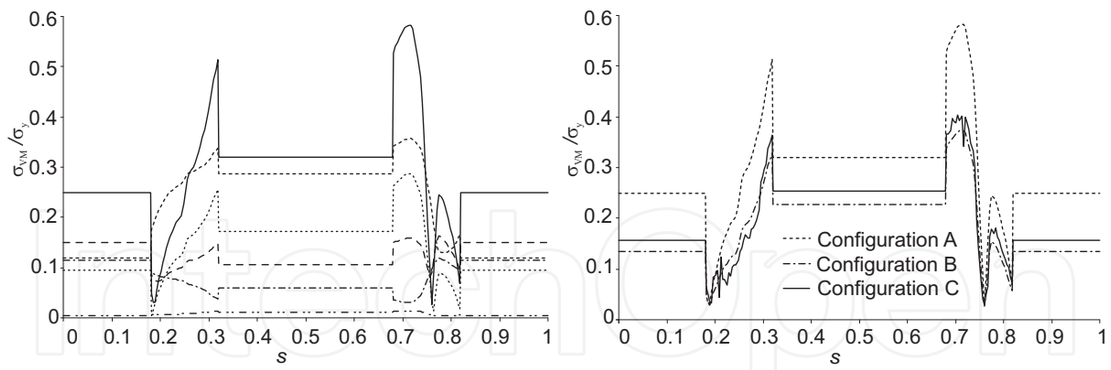

(a) (b)

Fig. 12. Von Misses yielding stress ratio in function of the parametric position along the path. (a) Configuration A. (b) Comparison of the maximum stress for Configurations A, B, and C. Data for Configuration C also include the oscillating stress component due to rail imperfections.

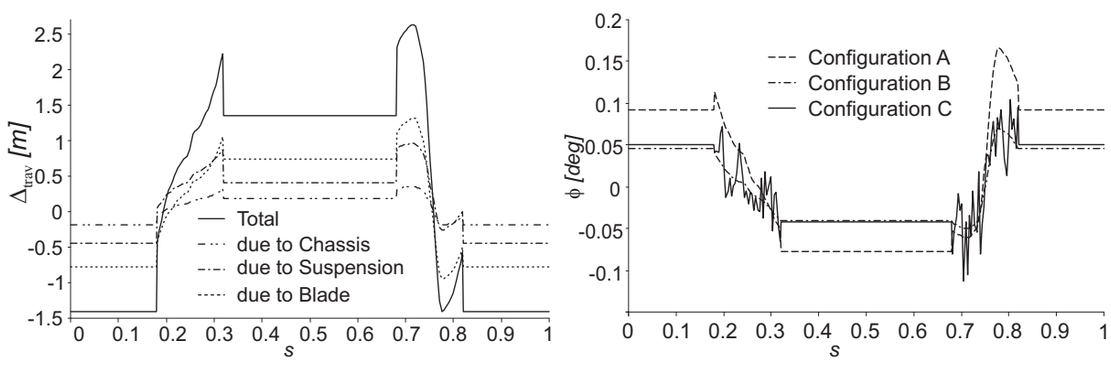

(a) (b)

Fig. 13. Blade-tip transverse displacement in function of the parametric position along the path. Configuration A (a). Comparison of blade-tip torsion angle in function of the parametric position along the path for configurations A, B and C. Data for Configuration C include the oscillatory effect induced by rail imperfections (b).

and 11(b). The latter modification substantially increased the torsional stiffness of the chassis. This reduction of the wagon's torsion translates into a reduced roll, and then decreases the chassis contribution to blade-tip displacement. The combined effect of these modifications to the three major structural components reduced the total transverse blade-tip displacement by 20%.

The global behaviour shown by Configuration B was satisfactory, but we were looking for a more compact design for the chassis in order to reduce the investment in materials and especially the cost of civil works. To this end, we reduced the distance between the railroads in 3 meters by cutting the 1.5-meter stubs that connect the transverse arms with the suspensions on each side of Configuration B. Thus, we arrived to Configuration C, which combines the satisfactory global behaviour of its predecessor with compactness of construction, and constitutes a somehow definitive design. At this point, we introduced in our simulations

the effect of rail imperfections. Figure 12(b) shows the maximum stress along the path for Configuration C when rail imperfections are present. It is clear that stress fluctuations induced by the imperfections are relatively small compared with the overall stress, without load peaks that may compromise structural integrity by fatigue.
Another important aspect substantially improved by the new configuration was the reduction of the blade-tip torsion angle, which can be seen in figure 13(b) where a comparison of this parameter among the designs is shown. The absolute value of ϕ for Configuration B is smaller than 0.07 degrees; and when the effect of rail imperfections is included, this value does not exceed 0.12 degrees. This result proved to be important because, before starting this study, we considered the possibility of feeding-back the torsion angles at each point along the blade to recalculate aerodynamic forces. Now, in view of the fact that the fluctuations in blade torsion angle are very small in terms of the optimum angle of attack (which is the angle of attack in normal operation), we may discard the effects of blade torsion in future calculation of the aerodynamic forces.

4. Analysis of the dynamical response of the suspension system

In this section, we shall focus on the problem of the suspension system, considering its interaction with the other two systems according to the following hypothesis: One, the reticulated structure of the wagon chassis acts as a rigid body (i.e. its stiffness is high compared with the suspension's); two, the link between the bearing of the blade and the wagon is rigid; three, the mass of the springs and dampers is negligible compared to the mass of the whole blade-wagon.
In order to compute the inertia tensor and mass of the blade-wagon, we first generate a three-dimensional mesh of isoparametric finite elements, each one representing one beam of the reticulated structure of the chassis. The same meshing code was used to discretize the blade as a series of variable-section beam finite elements. This provides the necessary data to obtain the inertia tensor and the loads for the chassis and the blade by the classical process of numerical integration used in the finite element method. We did not solve a finite element problem, but used the finite-element interpolation functions and integration techniques. By rotating and relocating each single element in the structure, we were able to calculate its inertia tensor and applied load, and referred them to a global coordinate system. We chose the point where the blade is linked to the chassis as the reference point because of its very high stiffness compared to the rest of the structure. To obtain the mass of the blade-wagon, we simply integrated the volume of each element applying the corresponding density according to a materials database.
Given a mass system in which the position of its particles is referred to a local coordinate system (x_1, x_2, x_3), the inertia tensor for the mass system, referred to the origin, is represented by the matrix:

$$I = \begin{bmatrix} I_{11} & I_{12} & I_{13} \\ I_{21} & I_{22} & I_{23} \\ I_{31} & I_{32} & I_{33} \end{bmatrix}. \tag{29}$$

The elements on the diagonal I_{11}, I_{22}, I_{33} are the axial moments of inertia referred to the x_1, x_2, x_3 axes. The elements outside of the diagonal are called the centrifugal moments of inertia

with respect to each pair of axes. Being the inertia tensor a symmetric matrix, we have: I_{12}=I_{21}, I_{23}=I_{32}, I_{13}=I_{31}. The expresion for each element is:

$$\begin{aligned} I_{11} &= \int \left(x_2^2 + x_3^2\right) dm & I_{12} &= \int (x_1\, x_2)\, dm \\ I_{22} &= \int \left(x_1^2 + x_3^2\right) dm & I_{23} &= \int (x_2\, x_3)\, dm \\ I_{33} &= \int \left(x_1^2 + x_2^2\right) dm & I_{13} &= \int (x_1\, x_3)\, dm \end{aligned} \tag{30}$$

Alternatively, each element can be also expressed by:

$$I_{ij} = \int \left[\left(\sum_{k=1}^{3} x_k^2 \right) \delta_{ij} - |x_i x_j| \right] dm \tag{31}$$

where δ_{ij} is a scalar of the form

$$\delta_{ij} = 1 \qquad \text{if } i = j, \qquad\qquad \delta_{ij} = 0 \qquad \text{if } i \neq j.$$

The evaluation of these integrals in the inertia tensor and the mass of the blade-wagon was done by using the interpolation functions and numerical integration rule for isoparametric three-node one-dimensional finite elements. A detailed description of these functions and the isoparametric technique may be found in Bathe (1996). Once the inertia tensor of each element has been calculated on its local coordinate system, we relocate it by using Steiner's Theorem with the blade-chassis link as the reference point. Once we have the element in its corresponding location in the structure and referred to a global coordinate system, we obtain the inertia tensor of the complete structure by applying the same process to the rest of the elements.

The new components on the inertia tensor can be defined as:

$$\begin{aligned} I_{11st} &= I_{11} + m\left(y'^2 + z'^2\right) & I_{12st} &= I_{12} + m\,(x'y') \\ I_{22st} &= I_{22} + m\left(x'^2 + z'^2\right) & I_{23st} &= I_{23} + m\,(y'z') \\ I_{33st} &= I_{33} + m\left(x'^2 + y'^2\right) & I_{13st} &= I_{13} + m\,(x'z') \end{aligned} \tag{32}$$

$$x' = |x_{global} - x_{ref}| \qquad y' = |y_{global} - y_{ref}| \qquad z' = |z_{global} - z_{ref}|$$

From the aerodynamic study, described in section 2, we have data about the optimum value for the blade pitch angle for a discrete number of positions along the trajectory. These data were used to compute the exact value of the inertia tensor in those positions, which depends on the relative angle between the blade and the chassis. Finally, we obtain a continuous expression for each component of the inertia tensor along the trajectory using a spline interpolation between those discreet positions.

We compute a solution for the time-dependent dynamics by solving the system of ordinary differential equations (ODE) for the blade-wagon as a body. Once we have the solid body modeled with its correspondent inertia tensor and the loads, we proceeded to solve the conservation of the linear momentum in axis y and z, and the angular momentum in the three dimensions. It involved the solution of an ODE system of five equations, which gives us

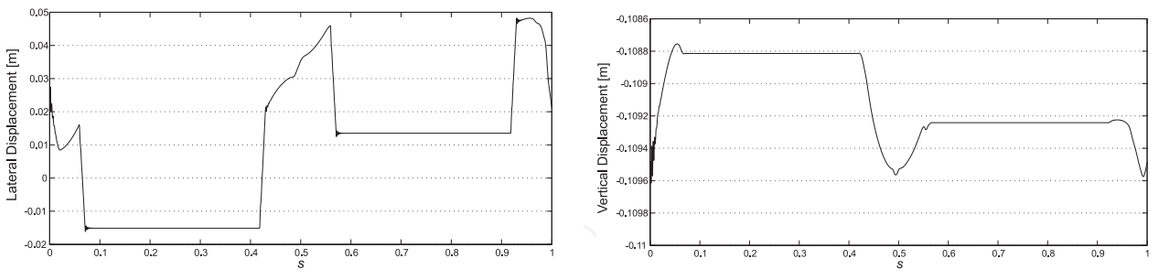

(a) (b)

Fig. 14. Displacements of the blade wagon at the point of the blade-chassis link: lateral direction (a), vertical direction (b).

the displacements and rotations of the blade wagon referred to the blade-chassis link (i.e. the *reference point*). Once we have these displacements and rotations, computing the loads on the springs and shock absorbers in the suspension system is straightforward. Finally, these will give us the crucial information about the normal and tangential loads exerted on the rails as for each position along the trajectory.

The original ODE system of five second-order equations was first transformed into an equivalent system of ten first-order equations using the change-of-variables technique. Then, the transformed system was solved by a multivalue variable-order predictor-corrector solver with adaptive stepsize control. The whole set of three subroutines was written in the MATLAB language.

4.1 Numerical results

In this section we show the numerical results of a series of tests we conducted on a typical VGOT configuration (Ponta & Lago, 2008). Vertical spring stiffness is $4.9370 * 10^6$ N/m, lateral spring stiffness is $3.5737 * 10^6$ N/m, and shock-absorber stiffness in both vertical and horizontal directions is 10^5 N/m. The pre-load of the lateral springs is 250 kN. We included a 110 kN ballast at the rear of the chassis to compensate the pitch moment induced by the aerodynamic *pushing* force applied at the center of pressure of the blade. This permanently acting pitch moment is inherent to the normal operation of the blade-wagon and the use of the ballast is a simple and practical solution to compensate it. The blade height is 50 m; its airfoil section has a chord length of 8 m at the base and 4 m at the top. The thickness of the fiberglass composite shell that forms the blade structure is 0.1 m at the base and 0.01 m at the top. We used a mesh of 1453 finite elements to model the reticulated structure of the chassis, and a mesh of 50 beam elements of variable section to discretize the blade.

Figure 14 shows the displacements of the blade wagon at the point of the blade attachment onto the chassis: In the lateral direction 14(a), and in the vertical direction 14(b). Figure 15 shows the angular motions of the blade-wagon: Roll 15(a) and Pitch 15(b). Figure 16 shows the loads on the springs along the trajectory: In the lateral direction 16(a), and in the vertical direction 16(b). Finally, Figure 17 shows the loads on the shock-absorbers along the trajectory: for the lateral 17(a), and vertical direction 17(b).

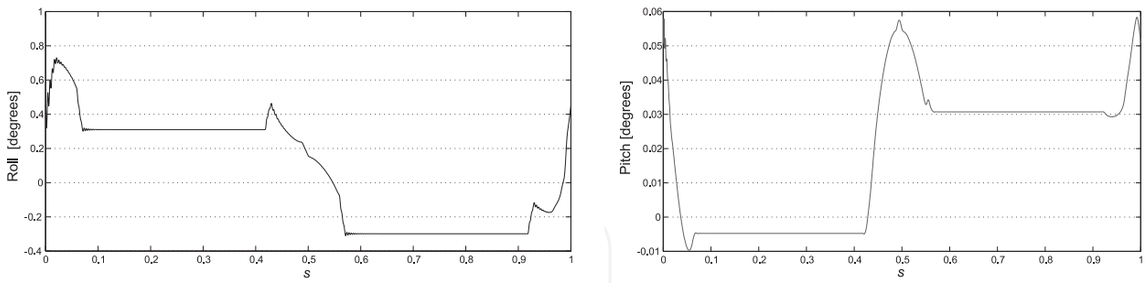

(a) (b)

Fig. 15. Angular motions of the blade-wagon: roll (a), and pitch (b).

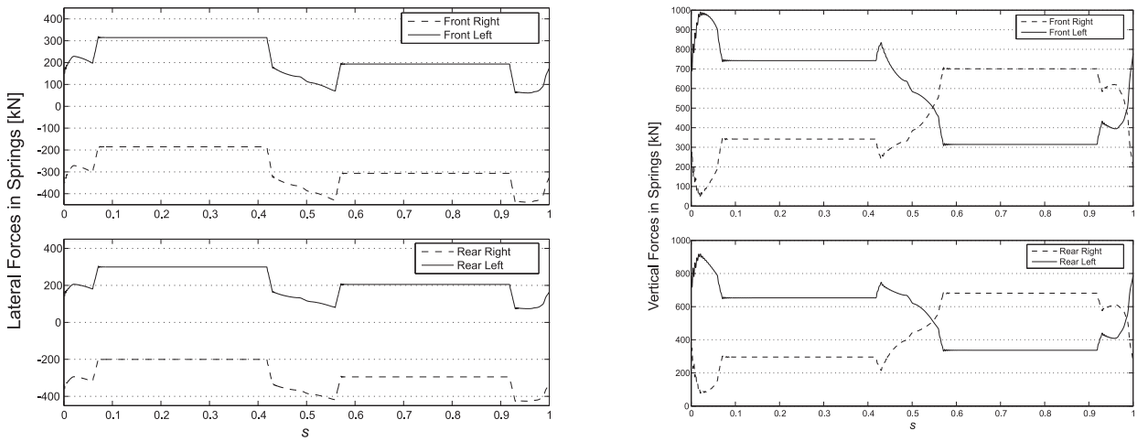

(a) (b)

Fig. 16. Loads on the springs along the trajectory: lateral (a), and vertical direction (b).

5. Concluding remarks

A good evaluation of the actual economic efficiency of the VGOT as an energy-conversion system must take into account the savings in investments due to the substantial reduction in the number of blades and railway length due to the adoption of an oval shape. As it is logical to expect, for the unfavorable cases where the wind shows a preferential bearing aligned with the oval's mayor axis, efficiency is appreciably smaller than for a standard rotor and it keeps decreasing with CF. However, this last situation will never occur in reality because nobody would design a trajectory layout in such a way that its mayor axis is aligned with the wind's preferential bearing. Hence, the worst possible case of all reduces to a compass rose with no preferential bearing which could be dealt with simply by adopting an almost-circular trajectory.

We also have to keep in mind that, even in those cases when we were compelled to use a circular-trajectory layout due to the characteristics of the compass-rose, the advantages mentioned in Section 1 regarding the low-rotational-speed problems associated to a classical

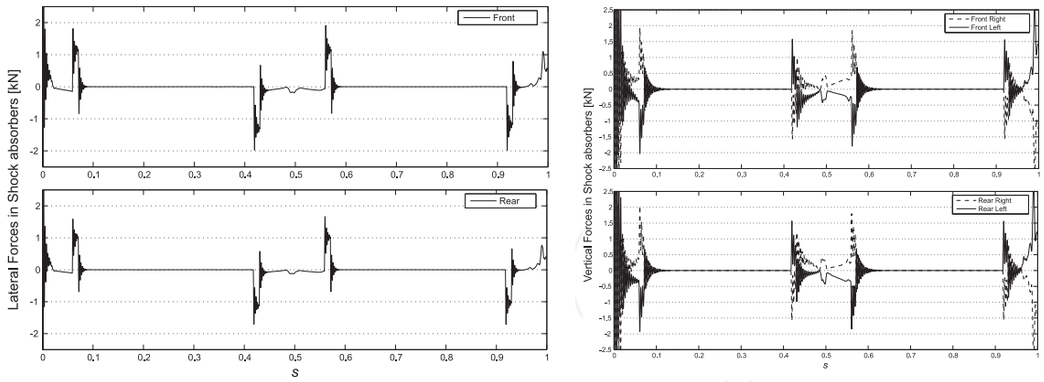

(a) (b)

Fig. 17. Loads on the shock-absorbers along the trajectory: lateral (a), and vertical direction (b).

Darrieus rotor of large diameter are still valid, as well as the possibility of using a blade-positioning control system that operates continuously during the cycle without the fatigue and mechanical-inertia problems associated to variable-geometry attempts in classical Darrieus rotors.

Results shown here indicate that our model possesses the capability to simulate the behavior of this unconventional layout, which expands the spectrum of analysis for Darrieus-turbine design. With this tool, we may determine the optimum values for the layout, the structural configuration, and the stiffness of the springs and shock-absorbers that would be adopted for the suspension system. This process would give us the right balance between the energy-conversion efficiency, the weight and cost of the structure, the stability of the blade-wagon during its normal operation, and the loads exerted on the rails. Excessive stiffness and weight would not only increase the costs of manufacturing but would also induce high loads on the rails and other components of the drive train (like wheels and bogies) compromising their durability.

In the present study, the rails were assumed as brand new (i.e. misalignments and surface degradation due to wearing were not taken into account), which would represent the original design conditions. In an extended version of our model, we shall include an additional subroutine that introduces random displacements on the wheels with the same statistical regularity of the misalignments and/or increased roughness due to natural ageing of the rails. This will allow us to simulate more realistic conditions in further stages of the plant's operational life.

6. Acknowledgements

F.P. is very grateful for the financial support made available by the National Science Foundation through grants CEBET-0933058 and CEBET-0952218.

7. References

Bathe, K. J. (1996). *Finite element procedures*, Prentice Hall, Englewood Cliffs, New Jersey, USA.
Burden, R. L. & Faires, J. D. (1998). *Numerical analysis*, Brooks Cole.

de Vries, E. (2005). Thinking bigger: Are there limits to turbine size?, *Renewable Energy World* 8(3).

Kwon, Y. W. & Bang, H. (1997). *The finite element method using Matlab*, CRC Press.

Manwell, J. F., McGowan, J. G. & Rogers, A. L. (2002). *Wind energy explained: Theory, design and application*, Wiley.

NREL (2005). Wind power today, *Report DOE/GO-102005-2115*, U.S. Department of Energy.

NREL (2008). 20% wind energy by 2030: Increasing wind energy's contribution to U.S. electricity supply, *Report DOE/GO-102008-2567*, U.S. Department of Energy.

Otero, A. D. & Ponta, F. L. (2002). Numerical results for the structural behavior of a blade element of a V.G.O.T. Darrieus, *VIIth World Renewable Energy Congress, Cologne*, Pergamon, p. 223.

Otero, A. D. & Ponta, F. L. (2004). Finite element structural study of the VGOT wind turbine, *Int. J. Global Energy Issues* 21: 221–235.

Paraschivoiu, I. (1982). Aerodynamics loads and performance of the Darrieus rotor, *J. Energy* 6: 406–412.

Paraschivoiu, I. (1983a). Double multiple streamtube model with recent improvements, *J. Energy* 7: 250–255.

Paraschivoiu, I. (1983b). Predicted and experimental aerodynamics forces on the Darrieus rotor, *J. Energy* 7: 610–615.

Ponta, F. L. & Lago, L. I. (2008). Analysing the suspension system of VGOT-Darrieus wind turbines, *Energy for Sustainable Development* 12: 5–16.

Ponta, F. L. & Luna Pont, C. A. (1998). A novel technique for high-power electricity generation in high-speed wind regimes, *Vth World Renewable Energy Congress, Florence*, Pergamon, pp. 1936–1939.

Ponta, F. L. & Otero, A. D. (2002). A 3-node isoparametric finite element model for structural analysis of the V.G.O.T. Darrieus, *VIIth World Renewable Energy Congress, Cologne*, Pergamon, p. 252.

Ponta, F. L., Otero, A. D. & Lago, L. (2004). The VGOT Darrieus wind turbine, *Int. J. Global Energy Issues* 21: 303–313.

Ponta, F. L., Otero, A. D., Luna Pont, C. A. & Seminara, J. J. (2001). Mechanical, structural and electrical concepts for the engineering of a V.G.O.T. Darrieus turbine, *2001 European Wind Energy Conference and Exhibition, Copenhagen*, WIP - Renewable Energies and ETA, pp. 599–601.

Ponta, F. L., Otero, A. D., Seminara, J. J. & Lago, L. I. (2002). Improved design for the structure and gear system of a blade element of a V.G.O.T. Darrieus, *VIIth World Renewable Energy Congress , Cologne*, Pergamon, p. 222.

Ponta, F. L. & Seminara, J. J. (2000). Double-multiple streamtube model for variable-geometry oval-trajectory Darrieus wind turbines, *VIth World Renewable Energy Congress, Brighton, U.K.*, Pergamon, pp. 2308–2311.

Ponta, F. L. & Seminara, J. J. (2001). Double-multiple streamtube model for V.G.O.T. Darrieus turbines with recent improvements, *2001 European Wind Energy Conference and Exhibition, Copenhagen*, WIP - Renewable Energies and ETA, pp. 410–413.

Ponta, F. L., Seminara, J. J. & Otero, A. D. (2007). On the aerodynamics of variable-geometry oval-trajectory Darrieus wind turbines, *Renewable Energy* 32: 35–56.

Seminara, J. J. & Ponta, F. L. (2000). Numerical experimentation about an oval-trajectory Darrieus wind turbine, *VIth World Renewable Energy Congress, Brighton, U.K.*, Pergamon, pp. 1205–1209.

Seminara, J. J. & Ponta, F. L. (2001). Numerical results for a V.G.O.T. Darrieus turbine for different wind compass-rose conditions, *2001 European Wind Energy Conference and Exhibition, Copenhagen*, WIP - Renewable Energies and ETA, pp. 406–409.

Strickland, J. H. (1975). The Darrieus turbine: a performance prediction model using multiple stream tubes, *Report SAND75-0431*, Sandia Laboratory.

Templin, R. J. (1974). Aerodynamic performance theory for the NRC vertical axis wind turbine, *Report LTR-LA-160*, National Research Council of Canada.

Wilson, R. E., Walker, S. N. & Lissaman, P. (1976). Aerodynamics of the Darrieus rotor, *J. Aircraft* 13: 1023–1024.

WWEA (2010). World wind energy report 2009, *Report*, World Wind Energy Association. `www.wwindea.org`.

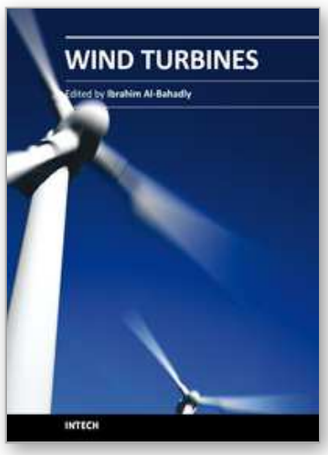

Wind Turbines

Edited by Dr. Ibrahim Al-Bahadly

ISBN 978-953-307-221-0
Hard cover, 652 pages
Publisher InTech
Published online 04, April, 2011
Published in print edition April, 2011

The area of wind energy is a rapidly evolving field and an intensive research and development has taken place in the last few years. Therefore, this book aims to provide an up-to-date comprehensive overview of the current status in the field to the research community. The research works presented in this book are divided into three main groups. The first group deals with the different types and design of the wind mills aiming for efficient, reliable and cost effective solutions. The second group deals with works tackling the use of different types of generators for wind energy. The third group is focusing on improvement in the area of control. Each chapter of the book offers detailed information on the related area of its research with the main objectives of the works carried out as well as providing a comprehensive list of references which should provide a rich platform of research to the field.

INTECH
open science | open minds

InTech Europe
University Campus STeP Ri
Slavka Krautzeka 83/A
51000 Rijeka, Croatia
Phone: +385 (51) 770 447
Fax: +385 (51) 686 166
www.intechopen.com

InTech China
Unit 405, Office Block, Hotel Equatorial Shanghai
No.65, Yan An Road (West), Shanghai, 200040, China
中国上海市延安西路65号上海国际贵都大饭店办公楼405单元
Phone: +86-21-62489820
Fax: +86-21-62489821

IntechOpen